

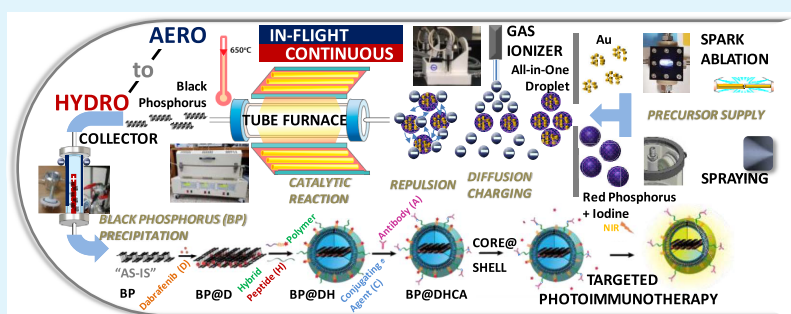
Method for the Instant In-Flight Manufacture of Black Phosphorus to Assemble Core@Shell Nanocomposites for Targeted Photoimmunotherapy

Hanh Thuy Nguyen,[†] Jeong Hoon Byeon,^{*,‡} Cao Dai Phung,[†] Le Minh Pham,[†] Sae Kwang Ku,[§] Chul Soon Yong,[†] and Jong Oh Kim^{*,†}

[†]College of Pharmacy and [‡]School of Mechanical Engineering, Yeungnam University, Gyeongsan 38541, Republic of Korea

[§]College of Korean Medicine, Daegu Haany University, Gyeongsan 38610, Republic of Korea

Supporting Information



ABSTRACT: Inorganic nanomaterial (INM)-based combination cancer therapies have been extensively employed over the past two decades because of their benefits over traditional chemo- and radiotherapies. However, issues regarding the toxicity and accumulation of INMs in the body have arisen. This problem may be improved through the use of biodegradable or disintegrable nanosystems such as black phosphorus (BP). Challenges to the manufacture of fully nanodimensional BP remain. In addition, improvements in recently developed cancer immunotherapies require their incorporation with drugs, targeting agents, and delivery vehicles. With these needs in mind, this study develops a method for instant in-flight manufacture of nanodimensional BP using plug-and-play devices for subsequent assembly of photoimmunotherapeutic core@shell composites containing mutated B-raf inhibitors (dabrafenib), immune checkpoint inhibitors (PD-L1), and cancer-targeting antibodies (CXCR4). The resulting nanocomposites exhibited cancer targetability and regulatability of PD-L1 expression both in vitro and in vivo. These activities were further increased upon near-infrared irradiation due to the incorporation of a phototherapeutic component. These results suggest that these nanocomposites are promising as a new class of advanced cancer therapeutic agents.

KEYWORDS: combination cancer therapies, black phosphorus, instant in-flight manufacture, plug-and-play devices, photoimmunotherapeutic core@shell composites

The limitations of traditional cancer chemo- and radiotherapies have ignited extensive research on nanotherapeutics made from a variety of nanomaterials (NMs) to target cancers, deliver drugs, and stimulate antiproliferative processes.¹ Numerous approaches to developing stimuli-responsive modalities with enhanced permeability and retention (EPR), effectiveness, and targetability have been reported using inorganic NMs (INMs) (e.g., iron oxide, silica, gold [Au], carbon, and quantum dots).^{2,3} Because the size, morphology, surface, porosity, and functionality of INMs can be modulated, they are particularly amenable to integration with drugs, proteins, and/or organic/polymeric moieties into nanocomposites for combination cancer therapies.^{3,4} Two-dimensional materials (graphene and its derivatives, transition-metal dichalcogenides, palladium sheets, and Xenes) as INMs are also used for combination cancer therapies due to their

workable modalities and biocompatibility.⁵ Even though INMs provide practical advantages for the clinical translation of cancer nanotherapeutics, further investigations and optimization are needed to produce safer INMs and to develop suitable platforms for the continuous manufacture of nanotherapeutics.^{2,3,6}

All-in-one biodegradable or disintegrable nanosystems that contain INMs and other therapeutic agents have been introduced to enable the translation of INMs to clinics for safer and more efficient cancer nanotherapeutics.^{7,8} These nanoarchitectures allow for both efficient penetration into tumors and rapid degradation or clearance from the body after

Received: March 14, 2019

Accepted: June 24, 2019

Published: June 24, 2019

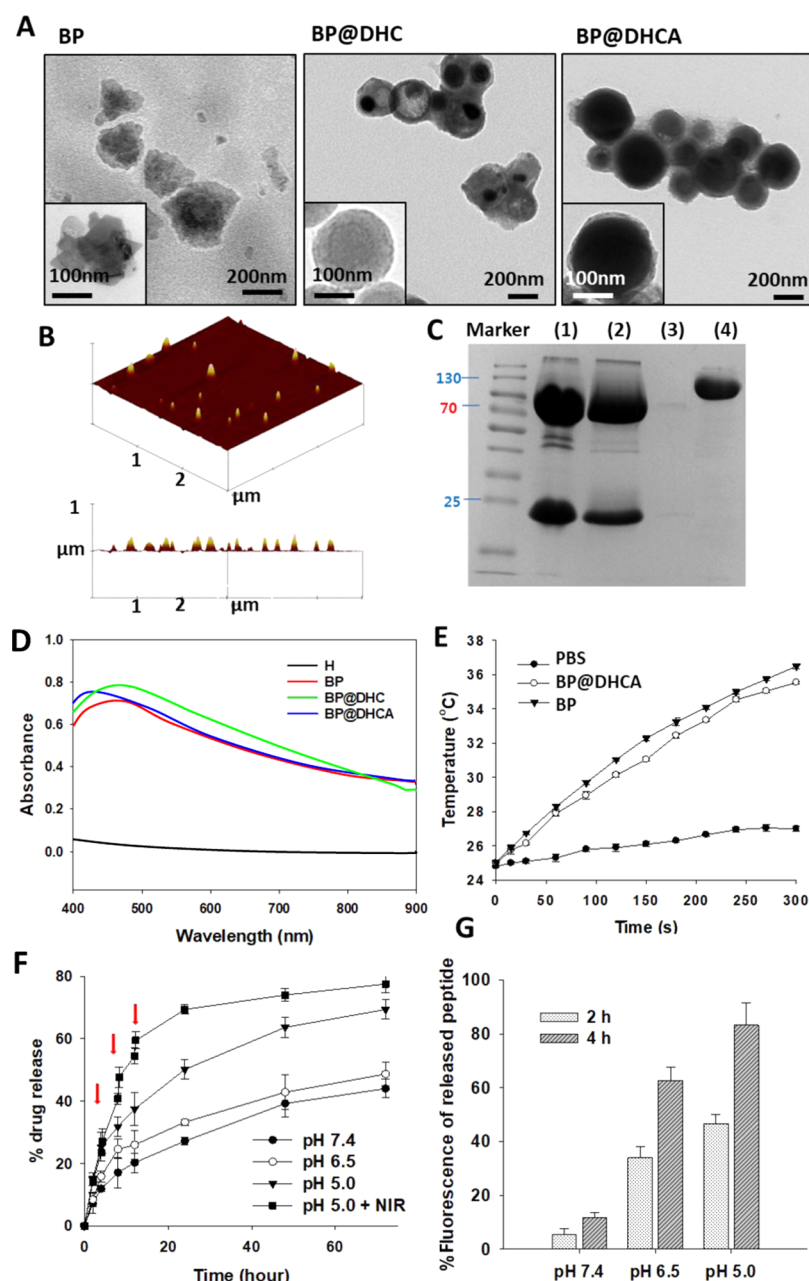


Figure 1. Characterization of BP@DHCA nanocomposites. (A) TEM images of BP@DHCA (right), including BP (left) and BP@DHC (middle). Specimens were prepared by dripping dispersion (BP [TEM images of in-flight manufactured BP before dispersing in PBS are displayed in Figure S1C], BP@DHC, or BP@DHCA in PBS at 25 $\mu\text{g/mL}$) on a carbon-coated copper grid and subsequent drying. (B) AFM topograph of BP@DHCA. The specimen was prepared by dripping the dispersion (at 2.5 $\mu\text{g/mL}$; diluted to examine individual BP@DHCA nanocomposites) on an ultraflat mica plate and subsequent drying. (C) SDS-PAGE of BP@DHCA and free A under reducing conditions (lane 1: BP@DHCA and lane 2: free A) and nonreducing conditions (lane 3: BP@DHCA and lane 4: free A). A band at around 130 kDa in the lane 3 represents the molecular weight of free A. (D) UV-vis spectra of BP@DHCA dispersed in PBS (25 $\mu\text{g/mL}$), including H, BP, and BP@DHC. (E) Photoinduced temperature-increase profiles of BP@DHCA and BP under NIR irradiation (808 nm, 1 W/cm²). (F) In vitro D-release profiles from BP@DHCA under different pH conditions. Red arrows indicate NIR irradiation time points for pH 5.0 + NIR. (G) Percent fluorescence of released peptide (Cy5.5-labeled PD-L1) from BP@DHCA under different pH conditions.

therapeutic use. Black phosphorus (BP) is a potentially useful material for this purpose because of its biodegradability⁹ and biocompatibility,^{10,11} along with its unique properties, including direct band gap, a broad range of light absorption, and texture.¹² Lateral nanodimensional BP exhibits both photodynamic and photothermal activities in the visible and near-infrared (NIR) range to, respectively, generate reactive oxygen species (ROS) and high temperature for the promotion of cancer cell death and tumor destruction.^{13–15} On the other

hand, the large lateral size (several hundred nanometers to several micrometers) of BP induces cytotoxicity due to physical damage from interactions between BP and the cell membrane.¹⁶ This large size precludes deeper penetration into tumors and impedes the clearance from the body.^{17,18} Thus, special chemical exfoliations or pretreatments are required to produce lateral nanodimensional BP.^{18,19} However, after such treatment, unwanted rapid degradation of nanosized BP led to an insufficient cancer therapeutic effect upon administration.²⁰

Some cancer immunotherapies are used to activate the immune system to eradicate cancer cells.²¹ Checkpoint blockade and cell-based therapies have demonstrated durable anticancer activities (long-term cancer therapeutics) and the prevention of cancer recurrence and metastasis.^{22,23} While these therapies exhibit encouraging clinical responses, they are still in the early stages of development.²⁴ Further studies are needed to practicalize cancer immunotherapies. The selection of optimal NMs for incorporation with immunotherapeutic agents and the design of an effective architecture may be required to provide treatment durability, sufficient capacity for loading therapeutic agents, and stimulus reactivity to boost the immune system.^{22–24} A combination of immuno- and phototherapies has been recently introduced to synergize cancer immunotherapeutic activities.^{25,26} Thus, the engineering of biocompatible, biodegradable, and EPR- and intracellular endocytosis-enabled NMs is needed for broadening the applicability of combination cancer immunotherapies.^{12,24}

To this end, we developed an instant in-flight process for the manufacture of lateral nanodimensional BP as a base NM for the assembly of photoreactive, all-in-one nanoarchitectures for cancer photoimmunotherapy. To achieve a final architecture within the nanometer range (mostly <200 nm), the base BP (mostly <100 nm) was instantly manufactured in less than 16 s via a series connection of plug-and-play (digitizable) devices (spark ablation, mechanical spraying, negative gaseous ion generation, electrically heated tube reaction, and electrostatic precipitation) in a single-pass, continuous, in-flight configuration without the use of exfoliation or pulverization processes (Figure S1A). Specifically, Au nanoparticles (NPs) from spark ablation and negative gaseous ions from carbon brush ionization in a nitrogen gas flow were simultaneously injected as the operating fluid into the nozzle of a mechanical spray device filled with a solution of red phosphorus and iodine (RP + I), yielding negatively charged hybrid droplets of Au, RP, and I. These droplets were then passed through a heated tubular reactor for the thermal conversion of RP into BP in the presence of Au catalyst and I. After further passing through a diffusion dryer to eliminate residual vapors, the resulting BP nanopowders were electrostatically collected on a substrate in a positive electric field still in a single-pass gas stream. The BP powders were directly dispersed in a solution containing dabrafenib (D; B-raf inhibitor), hybrid polymer inhibitor peptide (H; programmed death-ligand 1 [PD-L1] linked with cholesterol–poly(ethylene glycol)–poly-L-lysine [CHO–PEG–PLL]), and vitamin E PEG maleimide (C; conjugating agent²⁷). Chemokine (C–X–C motif) receptor 4 (CXCR4) antibodies (A) were then conjugated to form the BP (core)@DHCA (shell) nanocomposites. The core@shell architecture was developed because the passivation of BP with biomaterials was expected to minimize undesirable physical toxicities (side effects)²⁸ and rapid degradation of naked BP.²⁹ The DH configuration was selected in this study because of the upregulation of PD-L1 on cancer cells following B-raf inhibition that induces lower toxicities in anti-PD-1/PD-L1 therapy compared with anticytotoxic T lymphocyte (CTL)-associated antigen-4 therapy.^{30,31} Antibody A effectively targets malignant colorectal, liver, and breast cancers^{32–35} and was thus adopted as a targeting agent through conjugation between the thiols of A and maleimides of C. The photoimmunotherapeutic efficacy of the assembled BP@DHCA nanocomposites was investigated in vitro and in vivo.

RESULTS AND DISCUSSION

To examine the conversion of RP into BP, the in-flight size distributions of Au NP, RP + I droplet, Au-RP + I droplet, and BP were measured using a scanning mobility particle sizer (SMPS), as shown in Figure S1B. The distribution of Au-RP + I exhibited a unimodal character (similar to RP + I droplet) upon incorporation of Au NPs (from spark ablation) and RP + I droplets (from mechanical spraying), indicating that all Au NPs were quantitatively combined with RP + I droplets to form Au-RP + I droplets. A significant shift in droplet size distribution from 154.3 nm (geometric mean diameter, GMD), 1.96 (geometric standard deviation), and 7.0×10^6 particles/cm³ (total number concentration) to 71.5 nm, 1.74, and 2.8×10^6 particles/cm³, respectively, occurred upon passing through the heated tubular reactor through solvent evaporation and subsequent catalytic conversion of RP. This result indicates that RP was thermally catalytically converted to lateral nanodimensional BP. The formation of BP was observed using a transmission electron microscope (TEM), and the BP was deposited via direct electrostatic collection immediately after passing through the diffusion dryer. The particles on a TEM grid mostly exhibited sizes smaller than 100 nm (73.6 ± 5.1 nm; measured 200 particles) in the lateral dimension (Figure S1C), which is consistent with the GMD measured by SMPS. A high-magnification TEM image shows lattice fringes of 0.341 and 0.234 nm, which match the (021) and (111) planes of BP and Au, respectively. This finding indicates that the in-flight thermal reaction of RP in the presence of Au NPs yielded nanodimensional BP and the catalysts (Au NPs) for the conversion remained as ultrasmall dots (<5 nm, renal clearable; measured 200 Au dots) on the surface of BP. Temperature elevation of the manufactured BP dispersed in phosphate buffered saline (PBS, pH 7.4) under NIR (808 nm) laser irradiation (3 min) was measured as a function of BP concentration using a thermal camera (Figure S1D). The photothermal activity of the BP for the elevations was comparable to that of previous reports in which Au-incorporated BP exhibited higher activity than naked BP.^{36,37} In addition, the rate of in vitro degradation of the manufactured BP was 3.7 mass percent per day. Thus, this finding warrants further investigation of the use of BP for photoimmunotherapeutic applications.

The architecture of the BP@DHC and BP@DHCA formed from the manufactured BP was observed via TEM (Figure 1A). Specimens of BP, BP@DHC, and BP@DHCA were prepared by dripping the dispersions on TEM grids and subsequent drying in a dust-free atmosphere. The lateral dimension of BP increased through its coagulation in the dispersion owing to its higher concentration in the dispersion than in the gas-phase. However, the hydrodynamic diameter of the dispersed BP measured using a dynamic light scattering (DLS) system remained as 173.1 ± 5.4 nm (Table S1). The incorporation of DHC and BP (before conjugation with A) changed the shape from flakes (naked BP) to spheres, and the gradation of asymmetries of the spherical particles represented the formation of the core (BP)@shell (DHC) architecture from the hydroreaction between BP, D (described in Table S1), H (described in Figure S2), and C. Although the conjugation of A with BP@DHC to form BP@DHCA nanocomposites further increased the size from 228.9 ± 0.6 to 235.9 ± 7.2 nm (Figure S3A), the gradation of the particles was more uniform than that of BP@DHC. The ζ -potential also changed

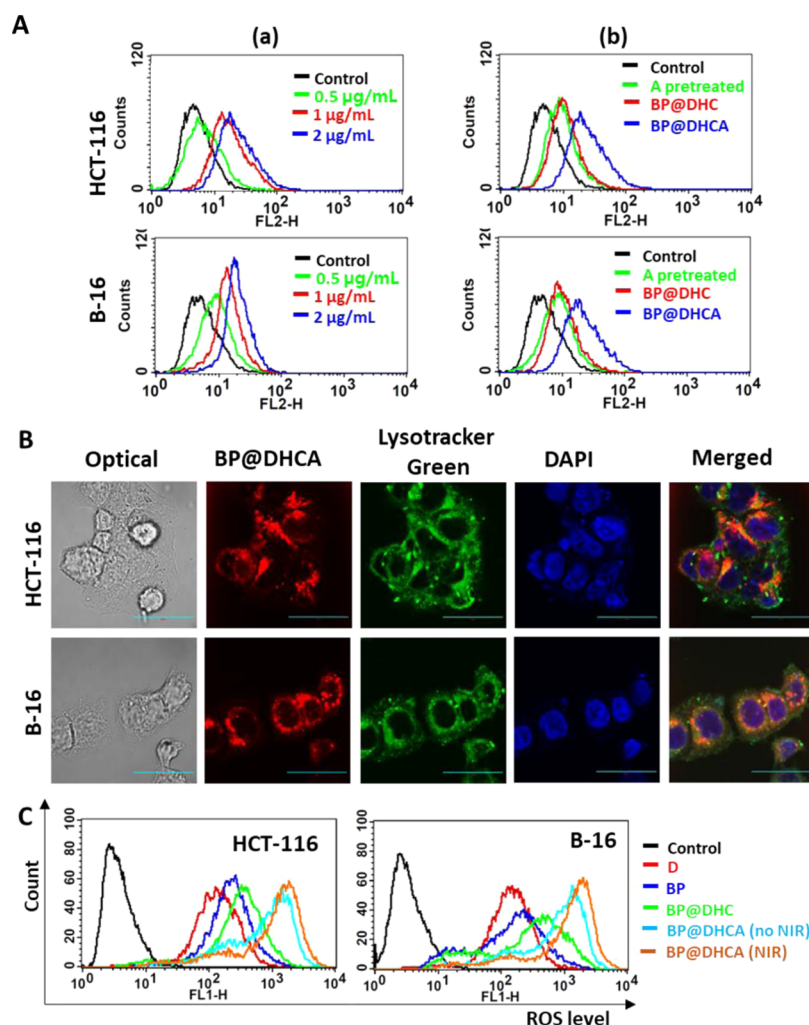


Figure 2. BP@DHCA nanocomposite uptake and subsequent ROS generation in HCT-116 and B-16 cancer cells. (A) Intracellular uptake for 1 h incubation with BP@DHCA at different D concentrations (a) and different treatment conditions (1 $\mu\text{g/mL}$ D for BP@DHC and BP@DHCA without NIR) with and without A pretreatment for 1 h at 20 $\mu\text{g/mL}$ free A (b). (B) Confocal images of cells treated with BP@DHCA (without NIR) (scale bar, 30 μm). LysoTracker Green and DAPI were used to determine the location of BP@DHCA in cellular compartments. (C) ROS generation of cancer cells treated with BP@DHCA in the absence and presence of NIR irradiation (1 W/cm^2 , 5 min). Intracellular generation is compared with that of free D, BP, and BP@DHC.

from -23.4 ± 0.9 to -21.9 ± 1.1 mV, as described in Table S1. Together, these findings indicate that A uniformly conjugated with BP@DHC, with the maintenance of the spherical shape. Coexistence of phosphorus (P) and carbon (C) in a single BP@DHCA was also examined using energy-dispersive X-ray (EDX) mapping, where C spots are distributed on the core P (Figure S3B). This morphological characteristic was more evident in a 10-fold dilution of the dispersion, which prevents capillary aggregation of the particles during drop-drying, during specimen preparation for atomic force microscopy (AFM). As shown in Figure 1B, the individual dots of BP@DHCA nanocomposites (~ 200 nm) were well distributed. The conjugation of A on BP@DHC was further validated via sodium dodecyl sulfate polyacrylamide gel electrophoresis (SDS-PAGE) (Figure 1C). Unlike reducing conditions (lane 1: BP@DHCA and lane 2: free A), under nonreducing condition for BP@DHCA (lane 3), no band was present representing the free A fragments, suggesting that the binding of A to BP@DHC was stable. The conjugation efficiency of this complex was $71.6 \pm 1.2\%$. The light absorption spectrum of naked BP analyzed using ultraviolet–

visible (UV–vis) spectroscopy was not significantly altered upon the DHC or DHCA incorporation (Figure 1D), demonstrating the potential photoreactivity of the nanocomposites over a broad spectrum of light. This broad spectral absorption (even includes >900 nm) may be because of plasmonic coupling between the BP and Au,³⁸ demonstrating an extendability for use in different NIR windows.³⁹ NIR irradiation of the nanocomposite dispersion resulted in temperature elevation comparable to that of naked BP (Figure 1E), and the resulting spectrum matched the light absorption spectrum of the nanocomposite. pH-responsive D release was examined at pH 7.4, pH 6.5, and pH 5.0 to simulate the release behaviors of D from BP@DHCA in normal and tumor microenvironments. The release was increased by decreasing the medium pH (reaching $64.4 \pm 4.1\%$ cumulative release), which was further increased ($75.6 \pm 2.7\%$ after 72 h) by NIR irradiation (1 W/cm^2 , 5 min) at the chosen time points. These results demonstrate that the complex possesses both pH- and photoresponsive modalities. The pH-responsive release of PD-L1 (inhibitor peptide) was investigated to confirm the suitability of BP@DHCA nanocomposites for tumor-selective

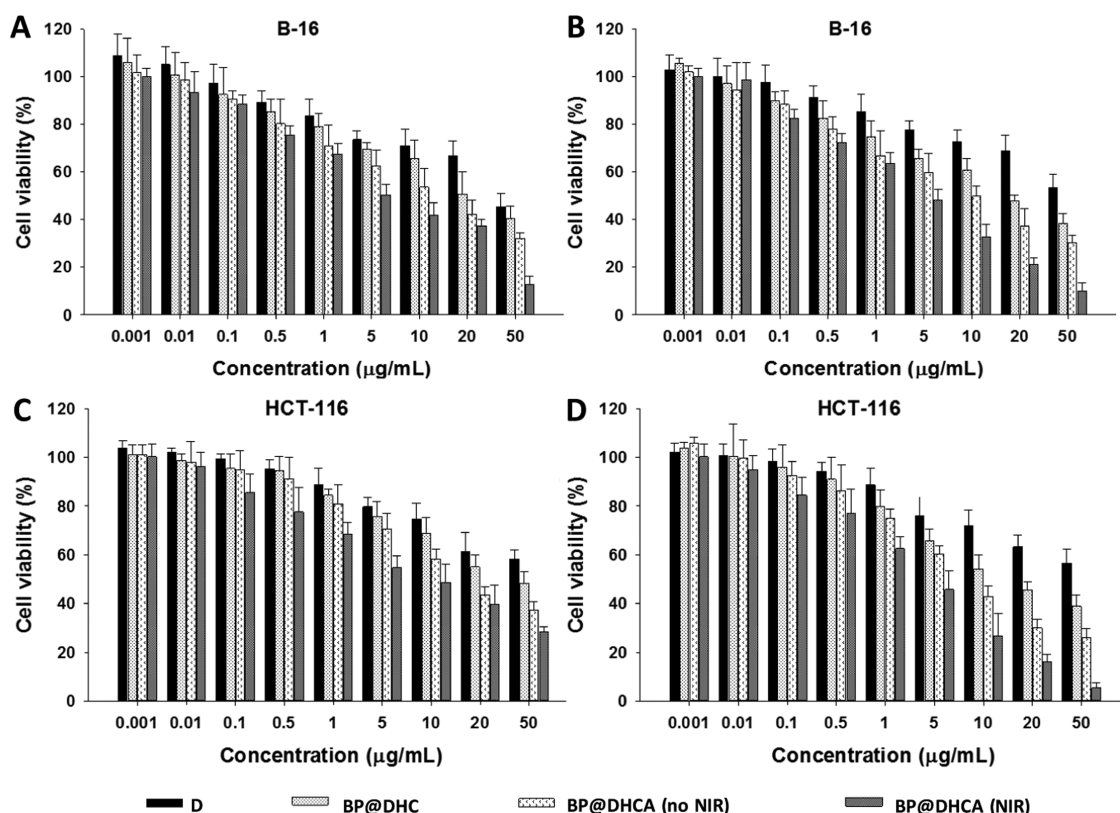


Figure 3. Cytotoxicities of BP@DHCA in cancer cells [(A, C) normally cultured; (B, D) co-cultured with CD8+ T cells] in the absence and presence of NIR irradiation, as compared to free D and BP@DHC. For BP@DHCA (NIR), cells were irradiated with an NIR laser (1 W/cm², 3 min) after 6 h incubation with BP@DHCA.

immunotherapy (Figure 1G). Cyanine 5.5 (Cy5.5)-labeled PD-L1 was included in the nanocomposites instead of PD-L1 to measure the amount of released peptide as fluorescence intensity. Upon a decrease in pH from 7.4 to 6.5, the fluorescence intensity increased significantly, likely due to cleavage of imine bonds at pH 6.5–6.8 through the protonation of PLL in H.^{40,41} This response may be suitable to release PD-L1 in the tumor extracellular environment, which has typically neutral to slightly acidic pH (6.5–7.0).⁴²

Intracellular uptake of BP@DHCA nanocomposites into HCT-116 (human colon cancer) and B-16 (murine tumor) cells was evaluated by fluorescence-activated cell sorting (FACS) and confocal microscopy. As shown in Figure 2A, BP@DHCA nanocomposite uptake into cells was dose-dependent (0.5–2 μg/mL of D). The targeting effect of A was examined by comparing the fluorescence intensities between cells treated with BP@DHC and those treated with BP@DHCA. The BP@DHCA exhibited greater uptake due to targeting by the conjugated A. This result was further confirmed by comparing the uptake of BP@DHCA nanocomposites with and without pretreatment of the cells with A, in which pretreatment saturates the CXCR4 receptors. The resulting decrease in BP@DHCA indicates that the complex enters the cells via the CXCR4/stromal cell-derived factor 1 chemokine receptor axis. To investigate the selectivity of BP@DHCA for cancer cells, the uptake of BP@DHCA into CD8+ T cells, isolated from C57BL/6 mice (confirmed by FACS analysis; Figure S4A), was evaluated. Under co-culture conditions (Figure S4B), the BP@DHCA nanocomposites exhibited greater uptake by cancer cells than did BP@DHC, whereas the uptake by CD8+ T cells did not differ significantly

between them. These results demonstrate that the BP@DHCA nanocomposites have a greater affinity for cancer cells than for CD8+ T cells. The viability of HCT-116, B-16, and CD8+ T cells treated with naked BP was estimated using the 3-(4,5-dimethylthiazol-2-yl)-5-(3-carboxymethoxyphenyl)-2-(4-sulphophenyl)-2H-tetrazolium (MTS) assay to assess biocompatibility (Figure S4C). The viability of the cancer cells and CD8+ T cells remained above 80% for all tested concentrations of BP, a result consistent with previous reports on the biocompatibility of Au-decorated BP.^{43,44} These results suggest that BP does not disrupt cell-selective uptake of BP@DHC or BP@DHCA. Confocal imaging (co-displayed with LysoTracker Green and 4',6-diamidino-2-phenylindole [DAPI] stained) further supports the significant uptake of BP@DHCA nanocomposites into cancer cells as evidenced by red fluorescence (Figure 2B). The production of a yellow color upon merging of the red fluorescence from the nanocomposites and green fluorescence from LysoTracker Green suggests internalization of the nanocomposites into acidic compartments of cancer cells. ROS generation in cells treated with BP@DHCA in the absence and presence of NIR irradiation was analyzed using FACS and was compared with other configurations (free D, naked BP, and BP@DHC), as shown in Figure 2C. Cells treated with the core@shell architectures BP@DHC and BP@DHCA exhibited greater ROS generation than did those treated with free D or naked BP, although free D and naked BP also generated ROS. This result might be because of the reduction in off-target distribution of D (refer to Figure 1F) by loading it onto the core@shell architectures. The difference in ROS generation between the core@shell architectures may result from their

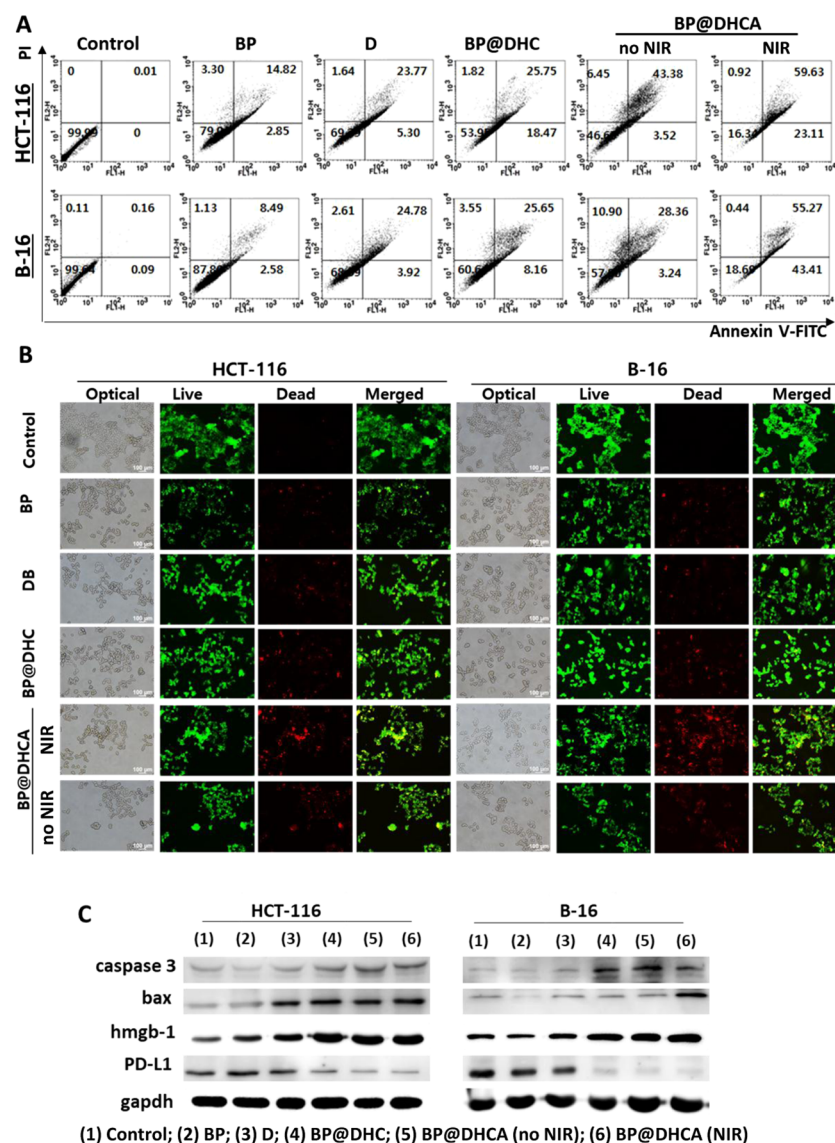


Figure 4. In vitro analysis of anticancer activity (HCT-116 and B-16 cells) of BP@DHCA (10 $\mu\text{g/mL}$) in the absence and presence of NIR irradiation, including BP, free D, and BP@DHC for comparison. (A) Apoptosis of cancer cells analyzed using Annexin V/PI kit. (B) Live/dead (scale bars, 100 μm) and (C) Western blot analyses. For BP@DHCA (NIR), cells were irradiated with an NIR laser (1 W/cm^2 , 3 min) after 6 h incubation with BP@DHCA.

different targetabilities. The phototherapeutic effect upon NIR irradiation (1 W/cm^2 , 5 min) further increased ROS generation in cells treated with the BP@DHCA nanocomposites, which might induce mitochondrial dysfunction and subsequent apoptosis of cancer cells.

The in vitro anticancer activity of BP@DHCA in the absence and presence of NIR irradiation was assessed by the MTS assay of HCT-116 and B-16 cells (Figure 3) comparing treatment with free D and BP@DHC at normal (A, C) and co-culture (B, D) conditions. The core@shell architectures exhibited greater cytotoxic effects on the cancer cells than did free D. The cytotoxicity was greatest for the BP@DHCA with NIR configuration due to its targeting and phototherapeutic effects. The cytotoxicities of the treatments were significantly lower in CD8⁺ T cells (Figure S4D) than in cancer cells, which may result from their cancer-cell-selective uptake. Treatment of the cancer cells with BP@DHCA or BP@DHC together with CD8⁺ T cells exhibited greater cytotoxic effects on the cancer cells than did treatment with the

nanocomposite alone, probably due to the additional cytotoxic effects of the T cells on the cancer cells (Figure 3B,D). NIR irradiation (1 W/cm^2 , 5 min) further increased the cytotoxic effect on the cancer cells, suggesting that the addition of this phototherapeutic effect on the cytotoxicity as photoimmunotherapy could further inhibit proliferation and survival of the cancer cells.

The proportion of apoptotic cells from the treatments was evaluated using the Annexin V kit (Figure 4A). Free D treatment of HCT-116 and B-16 cells induced late apoptosis of 23.77 and 24.78%, respectively, whereas treatments with BP@DHC at the same D concentration induced not only late apoptosis (25.75 and 25.65%) but also a significant early apoptosis (18.47 and 8.16%). While BP@DHCA without NIR induced significant necrosis and late apoptosis, BP@DHCA with NIR irradiation further increased the apoptotic fraction of cells. The level of dead cancer cells was further confirmed by staining with acridine orange/propidium iodide (Figure 4B). These results show that treatment with BP@DHCA with NIR

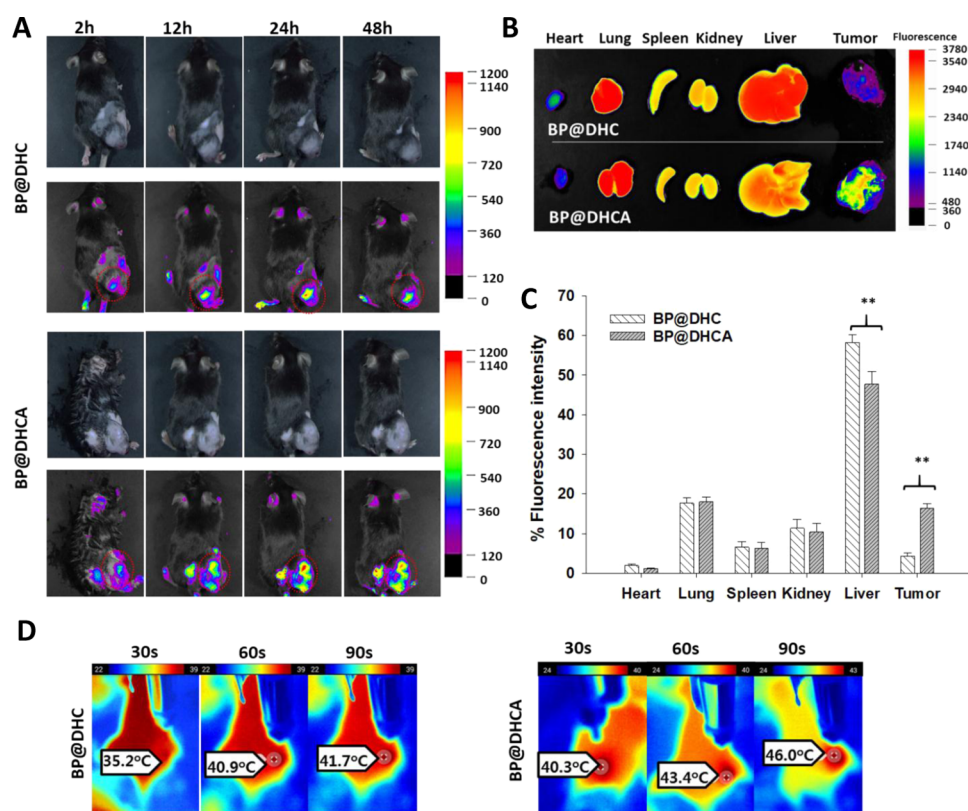


Figure 5. Biodistributions and photothermal activity of BP@DHC and BP@DHCA. (A) Fluorescence images of B-16 tumor-bearing mice for 48 h upon intravenous injection. (B) Fluorescence intensities and (C) percentages on major organs and tumor 48 h postinjection ($N = 3$, $**p < 0.01$). (D) Temperature contours of the tumor region under NIR irradiation (1 W/cm^2 , 3 min).

yields the highest levels of apoptosis, presenting the yellowish color in the merged images. These findings are consistent with the MTS and apoptosis assays, confirming the effectiveness of the photoimmunotherapy. Western blotting was also conducted to investigate apoptotic and immunogenic cell death upon treatment (Figure 4C), assessing the expressions of PD-L1, apoptotic marker proteins (cleaved caspase-3 and bax), and danger molecule (high-mobility group box 1 protein [hmgb-1]). The level of PD-L1 was significantly lower in cells treated with core@shell (BP@DHC or BP@DHCA) than in those treated with free D or naked BP. This result may be explained by the blockade effect of PD-L1 inhibitor peptides released from the core@shell nanocomposites via pH-responsive cleavage. Further FACS analyses (Figure S5) exhibited strong bindings between PD-L1 inhibitor peptide and PD-L1 in the two cell lines at a dose of $1 \mu\text{g/mL}$. Upregulation of cleaved caspase-3, bax, and hmgb-1 was observed in cells treated with core@shell nanocomposites as compared to those treated with free D or naked BP. NIR irradiation further increased this upregulation due to the additional phototherapeutic effects.^{45,46}

The in vivo distribution of the core@shell nanocomposites was assessed using Cy5.5 labeling (instead of the low dose treatment of individual dabrafenib) in B-16 tumor-bearing C57BL/6 mice (Figure 5A). Both nanocomposites were delivered to the tumor site with significantly greater accumulation in the area compared with that of free Cy5.5 (Figure S6A) even 48 h postinjection. Because Cy5.5 is rapidly eliminated from the body, the administration of free Cy5.5 resulted in very low fluorescence intensities in the whole body, organs, and particularly in tumors. The most intense

fluorescence at the tumor site was observed in BP@DHCA-treated mice, a result confirmed by ex vivo analysis of the fluorescence distribution in tumors and major organs after the mice were sacrificed (Figure 5B,C). The average fluorescence intensities in the tumor area of mice treated with BP@DHCA and BP@DHC were 16.43 ± 1.18 and $4.34 \pm 0.89\%$, respectively. The addition of A to the nanocomposite facilitated its selective binding to CXCR4 receptors on tumor cells, resulting in a significantly higher accumulation than that from BP@DHC. The greater accumulation of BP@DHCA at the tumor site thus resulted in a greater elevation in the temperature (locally irradiated area, Supporting Information) of BP@DHCA-treated mice (46.0°C) than in those treated with BP@DHC (41.7°C) upon NIR irradiation (1 W/cm^2 , 3 min) 24 h postinjection (Figures 5D and S6B [at 1 W/cm^2 , 90 s]).

The antitumor activities of naked BP, free D, BP@DHC, and BP@DHCA (with and without NIR) in the absence were compared by monitoring the tumor volume in B-16 melanoma cell allograft C57BL/6 mice (for ensuring proper matching between murine cancer cells and immune competent mice). As shown in Figure 6A, the tumors of mice in the control group developed rapidly. The volume was not significantly lower in mice treated with naked BP or free D than in controls, likely due to the biocompatibility of BP and nontargeted delivery of D, respectively. A noticeable decrease in tumor volume was seen upon DHC addition to BP, indicating that the combination of D and PD-L1 was required at least to induce significant antitumor activity. The tumor growth of mice treated with BP@DHCA in the presence of NIR was effectively inhibited (Figure S6C), without significant changes in body

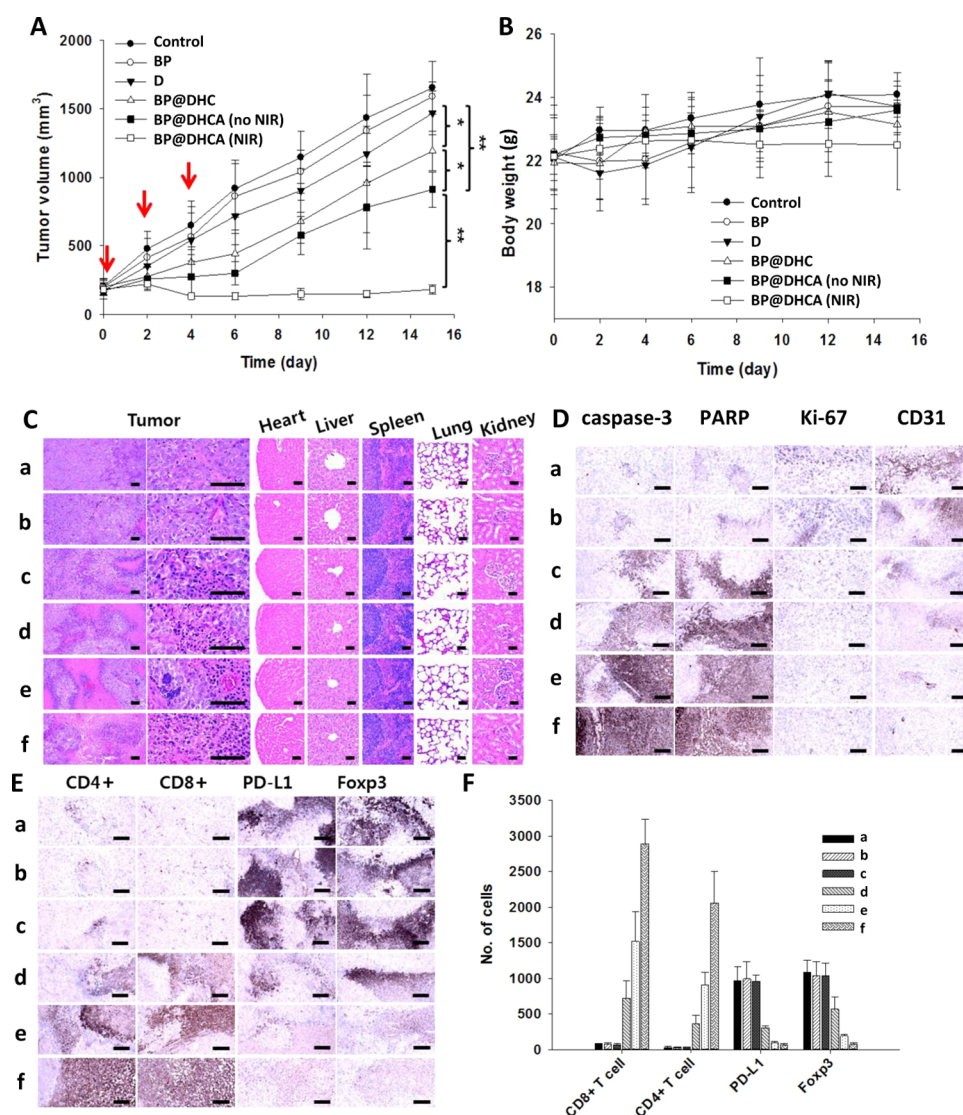


Figure 6. Potent antitumor activity of BP@DHCA in the absence and presence of NIR irradiation (1 W/cm^2 , 3 min, 6 h postinjection), including BP, free D, and BP@DHC against B-16 tumor-bearing C57BL/6 mice. (A, B) Time profiles of average tumor volumes and body weights of treated mice by group. Red arrows indicate the three time points of intravenous injection at 2 mg/kg ($N = 6$ mice for each treatment, $*p < 0.05$, $**p < 0.01$). (C) Representative sectional microscopic images (treated tumor and major organs) with H&E staining. Immunohistological analyses [(D) caspase-3, PARP, Ki-67, and CD31; (E) CD4+, CD8+, PD-L1, and Foxp3] in the tumor. (F) Number of immunolabeled cells in the tumor section upon the treatment. Panels a–f in (C)–(E) show the control, BP, free D, BP@DHC, BP@DHCA (no NIR), and BP@DHCA (NIR), respectively. Scale bars in (C)–(E): $120 \mu\text{m}$.

weight (Figure 6B). This improved antitumor activity derived from the addition of A to the composite, targeting delivery of D and PD-L1 to tumor cells and by exposure to NIR, which induces burst D release and the phototherapeutic effects of BP. No meaningful histopathological differences were observed in the major organs of all treated groups between treated and control mice (Figure 6C), suggesting therapeutic safety. Antitumor activity and organ integrity were further examined immunohistochemically in treated B-16 tumor-bearing C57BL/6 mice. The quantitative results of histomorphometrical analysis of tumor masses in mice treated with the different configurations (G1–G6) are shown in Table S2. Representative immunohistochemical images of tumor masses are displayed in Figure 6D,E. The comparative generation of cleaved caspase-3 and poly(ADP-ribose) polymerase (PARP), indicating apoptosis of tumor cells, was observed as BP@DHCA (NIR) > BP@DHCA (no NIR) > BP@DHC > free D,

whereas naked BP did not exhibit significant immunoreactivity. Correspondingly, attenuation of Ki-67 (proliferation marker) and CD31 (potent angiogenesis marker) was observed in the same order as the generation of caspase-3 and PARP. To specifically assess the effect of the nanocomposites on immune responses against the tumor in the absence and presence of NIR irradiation, the central area of the tumor mass was evaluated histologically to estimate the densities of CD4+, CD8+, PD-L1, and forkhead box P3 (Foxp3) (Figure 6F). A significant decrease in PD-L1 was observed in tumor masses of mice treated with DH-including configurations (BP@DHC and BP@DHCA), indicating effective inhibition generated by the release of PD-L1 from DH. An analogous decrease in Foxp3-immunolabeled cells was observed, whereas inverse tendencies were observed for CD4+- and CD8+-immunolabeled cells. These results indicate that the antitumor activity of the nanocomposites may occur through the inhibition of PD-

L1, T-cell-mediated immune stimulation, inhibition of tumor cell proliferation, and shutdown of angiogenesis. The addition of A or NIR onto DH-included configurations further increased the antitumor activity, which is consistent with the previous reports.^{47–49} This proves the efficacy of the photoimmunotherapy combination (A-mediated cancer targeting, D release, PD-L1 blockade, and BP-induced phototherapy) on B-16 tumor-bearing mice.

CONCLUSIONS

To efficiently assemble core@shell nanocomposites for targeted photoimmunotherapy, a method for the instant in-flight manufacture of lateral nanodimensional BP was developed to provide biosafe photoreactive core materials. The tumor-selective release of PD-L1 inhibitor peptides together with the phototherapeutic effects of BP (hyperthermia and burst D release) achieved downregulation of PD-L1 and induction of hmgb-1, resulting in a strong immune response against tumors. Furthermore, the biodegradable nanosystem architecture was stably tolerated in the treated mice, with no organ damage, indicating that instant in-flight manufacture of fully nanodimensional BP may provide a promising photoreactive platform for the assembly of photoimmunotherapeutic composites in the nanometer range.

METHODS

Instant In-Flight Manufacture of Lateral Nanodimensional BP

To manufacture lateral nanodimensional BP, a continuous, single-pass in-flight process constructed in five serially connected plug-and-play devices was designed, as shown in Figure S1A. The key reaction for formation of the fully nanoscale BP is the catalytic conversion of RP into BP under in-flight conditions filled with negative gaseous ions. The precursor for forming BP was prepared as a hybrid containing Au (catalyst), RP (P source), and I (reaction enhancer) droplet by incorporating Au NPs from spark ablation of two Au rods (AU-172561, Nilaco, Japan) and RP droplets (50 mL ethanol-based) (100 mg, Alfa Aesar) + I (3.5 mg, Sigma-Aldrich) created by mechanical spraying (0.3 MPa, operating pressure) through a nozzle (0.3 mm diameter). Negative gaseous ions generated by a carbon brush ionizer were also injected into the nozzle for diffusion charging of the droplets to induce electrostatic repulsion between the droplets (to prevent increased droplet size due to aggregation). The negative charge on the droplets for electrostatic repulsion was examined using a Faraday cage electrometer and found to be -145 ± 14.4 fA. These negatively charged droplets were injected into an electrically heated tubular reactor under 1.57 L/min of N₂ gas flow (15.5 s residence time) for deriving the in-flight conversion of RP into BP at 650 °C wall temperature in the presence of Au NPs and I molecules. After adsorbing residual vapors from the flow by passing through a diffusion dryer, BP was electrostatically collected as a powder in a rod-to-cylinder-type electrostatic precipitator operating at +2.5 kV/cm.

Preparation of H. CHO-PEG-NHS (Nanosoft Polymers) was dissolved in dimethyl sulfoxide (DMSO) at 1 mg/mL concentration, and acetal-PLL (Nanosoft Polymers) (2 mg/mL) in PBS (pH 7.4) was added to the CHO-PEG-NHS solution (2:1 molar ratio). The solution was stirred for 8 h and kept at 4 °C overnight to precipitate CHO-PEG-PLL. The precipitates were then washed and freeze-dried for further conjugation with the PD-L1 inhibitor peptide (Ar5Y_1 [FNWDYSWKSERLKEAYDL], Anaspec). The dried CHO-PEG-PLL was dissolved in 1 mL of DMSO at a concentration of 1 mg/mL and then diluted with 10 mL of PBS (pH 4.5) to convert the acetal into an aldehyde. The peptide was then linked with CHO-PEG-PLL (at 1:10 mass ratio) to form H through selective conjugation between the amine of the peptide and aldehyde groups in CHO-PEG-PLL. Excess reagents were removed using a Sephadex PD-10 column (GE Healthcare Life Science). H was collected by freeze-drying, and its chemical structure was examined using FITR

(Nicolet Nexus 670, Thermo Fisher Scientific) and ¹H NMR (DMX 300, Bruker, Germany) spectroscopies. To quantify the loaded peptides, peptides were first labeled with Cy5.5-NHS (Lumiprobe), and the amount of peptide released from H was determined using UV-vis spectroscopy (U-2800, PerkinElmer).

Preparation of BP@DHCA. To prepare the core BP, the H, D (Novartis), and C (PG2-MLVE-3k, Nanocs Inc.) DB were dissolved in methanol (6:1:3 mass ratio) and then evaporated in a vacuum rotary evaporator to yield DHC precipitates. BP nanopowders (1 mg) from the in-flight manufacture were dispersed in 10 mL of distilled water (final concentration 0.1 mg/mL) using a bath sonicator for 1 h. The DHC precipitates were dissolved in the BP dispersion under bath sonication for 30 min to form BP@DHC. The excess reagents were removed using a Sephadex PD-10 column, and the BP@DHC was collected by centrifugation. Conjugation of A (thiolated CXCR4 antibody; MBL International) to the surface of BP@DHC was conducted in PBS (pH 7.4) at a 1:50 molar ratio via the maleimide group of BP@DHC. The presence of D, H, C, and A components was confirmed by different methods. D concentration was determined using high-performance liquid chromatography (HPLC) that measures the unbound amount of D. After purification using a Sephadex PD-10 column, the fluorescence intensity induced from the Cy5.5-labeled H component was still observed from BP@DHC. A was conjugated on BP@DHC via the interaction between the thiol (in A) and maleimide (in C) groups, which was confirmed by SDS-PAGE. The reaction to yield BP@DHCA was performed at 4 °C for 4 h, and the BP@DHCA was purified using a Sephadex PD-10 column.

Physical Characterization. The size distributions of the product in gaseous and aqueous phases were measured using SMPS (3936, TSI Inc.) and DLS (Nano-ZS, Malvern Instruments, U.K.) systems, respectively. The negative charge current of the diffusion charged hybrid droplets was monitored using a Faraday cage electrometer (Charme, Palas GmbH, Germany). The surface charge and light absorbance were examined using DLS and UV-vis (T60, PG Instruments, U.K.), respectively. The morphologies were observed using a TEM (Tecnai G2 F20 S-TWIN, FEI) and an AFM (NanoscopeIIIa, Digital Instruments). Elemental analysis was also attempted using scanning electron microscopy (SEM)-EDX (S-4800, Hitachi, Japan) to examine the core@shell configuration. The photothermal activities were examined using a thermal camera (Therm-App TH, Opgal Optronic Industries Ltd., Israel).

Encapsulation and Release of D. The encapsulation of D to form BP@DHCA was estimated by measuring the amount of excess D in the dispersion. The free D was separated using a centrifugal filter (Amicon, MWCO 10 kDa, Millipore, Germany) and analyzed by HPLC equipment containing a reversed-phase column C18 (150 × 4.6 mm², 5 μm; GL Sciences Inc., Japan). The release profile of D from BP@DHCA was conducted in ABS (pH 5.0) and PBS (pH 6.5 and pH 7.4). The BP@DHCA dispersion (1 mL) was injected into a dialysis bag (Spectra/Por, MWCO 3500 Da; Spectrum Labs), which was then immersed in 30 mL of medium. The release was conducted at 37 °C and 100 rpm, and 1 mL of medium was withdrawn for D content measurements by HPLC at the chosen time points. To check NIR-induced D release, an NIR laser (1 W/cm²) was irradiated at 4, 8, and 12 h for 5 min.

In Vitro Anticancer Study. Cellular Uptake. The cellular uptake of BP@DHCA and BP@DHC nanocomposites into cancer and CD8+ T cells was determined using flow cytometry (BD FACS Calibur, BD Biosciences). Cy5.5 was first loaded onto nanocomposites to provide red fluorescence. Cancer cells were seeded onto 12-well plates (10⁵ cells/well) and incubated overnight. Cells were then treated with nanocomposites at different concentrations for 1 h. In the case of CD8+ T cells, the measurement was performed under co-culture conditions with cancer cells. Briefly, CD8+ T cells (5 × 10⁴ cells) were seeded onto 12-well Transwell plates (0.4 μm pores, Sigma-Aldrich) and co-cultured with HCT-116 cells (10⁵ cells). After incubation overnight, the cells were further incubated with nanocomposites for 1 h and harvested to estimate the uptake using FACS analysis. The intracellular uptake of nanocomposites into cancer cells was also confirmed using a confocal laser scanning microscope (K1-

Fluo, Nanoscope Systems, Korea). The cells were placed on a coverslip, incubated for 24 h, and treated with nanocomposites for 1 h. LysoTracker Green (1 $\mu\text{g/mL}$) was added and incubated for 10 min to stain the lysosome. After washing with PBS, the cells were fixed with 4% paraformaldehyde for 10 min, followed by staining with DAPI (1 $\mu\text{g/mL}$) for 5 min. The coverslip was mounted on a glass slide, and the cells were visualized using a microscope.

Cytotoxicity. The cytotoxicities of nanocomposites to cancer and CD8+ T cells were determined using the MTS assay. Briefly, 2×10^4 cancer cells per well were seeded onto 96-well plates (Becton Dickinson Labware) and incubated overnight at 37 °C. To examine the influence of immunogenic activity, cancer cells were co-cultured with an equal number of CD8+ T cells. The cells were then treated with the nanocomposites for 24 h. For BP@DHCA (NIR), NIR irradiation (1 W/cm^2 , 5 min) was applied to the cells after 2 h of treatment. After washing with PBS, the cells were added to 100 μL of PBS, followed by the addition of 20 μL of MTS solution (2 mg/mL) to estimate cell viability. Floating CD8+ T cells were collected in e-tubes and re-dispersed in 100 μL of PBS, followed by the addition of 20 μL of MTS solution (2 mg/mL). After 1 h incubation, absorbance was measured at 493 nm using a microplate reader (Multiskan EX, Thermo Scientific).

Live/Dead Assay. Cancer cells were seeded onto 12-well plates (2×10^5 cells/well). After incubation overnight to allow cell attachment, nanocomposites (10 $\mu\text{g/mL}$) were added. For the BP@DHCA (NIR) case, NIR irradiation (1 W/cm^2 , 5 min) was applied to the cells after 2 h of treatment. The cells were washed with PBS and stained with acridine orange and propidium iodide (Sigma-Aldrich) at concentrations of 6.7 and 750 μM , respectively. The live and dead cells were indicated by green and red fluorescence, respectively. Cell images were observed using inverted fluorescence microscopy (Eclipse Ti, Nikon, Japan).

ROS Generation. The levels of ROS generated in treated cells were evaluated by measuring DCFDA (Sigma-Aldrich) intensities. Cells were treated with nanocomposites (10 $\mu\text{g/mL}$) for 6 h and incubated with DCFDA (20 $\mu\text{g/mL}$) for 1 h. The cells were then washed twice with PBS and harvested to measure green fluorescence by FACS analysis.

Apoptosis. The PE-Annexin V/PI apoptosis kit (BD Biosciences) was used to evaluate cellular apoptosis after 24 h treatment with nanocomposites (10 $\mu\text{g/mL}$). Treated cells were washed with PBS and collected in a 5 mL tube. The cells were re-dispersed in 100 μL of binding buffer, followed by the addition of 5 μL of PE-Annexin-V and PI. After 15 min incubation in the dark, samples were adjusted to 1 mL volume by adding 1 \times binding buffer and analyzed by flow cytometry.

Cell Cycle. A cell-clock assay (Biocolor Ltd., U.K.) was used to determine the proportion of cells accumulated in each cell cycle phase. After treatment with nanocomposites (equivalent to 2 $\mu\text{g/mL}$ of D) for 24 h, the cells were washed twice with PBS, stained with 150 μL of cell-clock dye reagent, and incubated for 1 h. The cells were washed again with PBS and visualized using an optical microscope. The number of cells accumulated in G0/G1, S, and G2/M phases was quantified using ImageJ software, as indicated by the yellow, green, and dark-blue color, respectively.

Western Blotting. Cancer cells were seeded onto 12-well plates and treated with nanocomposites for 24 h. After treatment, the cells were harvested, re-dispersed in lysis buffer (M-PER, Thermo Fisher Scientific), and treated with ethylenediaminetetraacetic acid-free proteinase inhibitor (Roche Diagnostics). The proteins (40 mg) were then denatured by heating at 80 °C for 10 min, separated on a 10% SDS-PAGE gel operating at 80 V for 2 h, and transferred onto a poly(vinylidene fluoride) membrane (Millipore) at 210 mA for 90 min. After blocking in skim milk solution (5% in 1 \times Tris-buffered saline and 1% polysorbate 20 buffer), the membrane was incubated with purified primary antibodies against cleaved caspase-3, bax (Abcam), hmgb-1, PD-L1 (LifeSpan BioScience), and glyceraldehyde 3-phosphate dehydrogenase (gapdh; Santa Cruz Biotechnology) overnight, followed by incubation with appropriate secondary

antibodies for 1 h at room temperature. Luminol solution (Thermo Fisher Scientific) was finally added to visualize the proteins.

In Vivo Study. Biodistribution. Cy5.5-NHS was conjugated to the nanocomposites for the investigation of nanocomposite distribution in the body. B-16 tumor-bearing mice ($N = 3$) were intravenously injected with BP@DHCA or BP@DHC nanocomposites at 2 mg/kg . The nanocomposite distribution in the body was monitored for 48 h. On scarification of mice at 48 h, tumors and major organs were collected. The fluorescence images were captured using a fluorescence imaging system with NEOimage software (NeoScience, Korea).

Antitumor Effect. Nanocomposite administration into B-16 tumor-bearing C57BL/6 mice was started when the tumor reached 100–150 mm in size. The mice were randomly divided into six groups ($N = 6$) for the treatment at 2 mg/kg . The nanocomposites were injected on days 0, 3, and 6, and NIR irradiation (1 W/cm^2 , 5 min) was applied on the next day of injection only for the BP@DHCA (NIR) configuration. Tumor development was monitored by measuring the length (L) and width (W) of the tumor using a caliper. Tumor size was calculated as follows: tumor volume (mm^3) = $(L \times W^2)/2$.

Histological and Immunohistochemical Analyses. The tumor specimens and organs of B-16 tumor-bearing C57BL/6 mice treated with nanocomposites were separated, fixed in 10% neutral buffered formalin, and embedded in paraffin using an automated tissue processor (Shandon Citadel 2000, Thermo Scientific) and embedding center (Shandon Histocentre 3, Thermo Scientific). Samples were then sliced into 3–4 μm thick sections and stained with H&E.

Tumor cell markers for apoptosis (cleaved caspase-3 and PARP), angiogenesis (CD31), and cell proliferation (Ki-67) were examined using an avidin–biotin–peroxidase-based immunohistochemical stain using primary antisera. Changes in immunoreactivity in the tumor sections for CD4+, CD8+, PD-L1, and Foxp3 (a marker of regulatory T cell activity) were also assessed. The tumor cell volumes; mean cleaved caspase-3- and PARP-, Ki-67-, and CD31-immunolabeled cell percentages; and CD4+, CD8+, PD-L1-, and Foxp3-immunopositive cell numbers in tumor sections were calculated as %/ mm^2 using a computer-based image analysis program (iSolution FL ver 9.1, IMT i-solution Inc., Canada).

Statistical Analysis. Data are presented as the mean \pm standard deviation. Statistical significance was determined using one-way analysis of variance and two-tailed Student's t test. Differences were considered as significant for $p < 0.05$ (*) and very significant for $p < 0.01$ (**).

■ ASSOCIATED CONTENT

Supporting Information

The Supporting Information is available free of charge on the ACS Publications website at DOI: 10.1021/acsami.9b04632.

Plug-and-play BP manufacture; in-flight size distributions of Au NP, RP + I droplet, Au-RP + I droplet, and BP; TEM image and photothermal activity of manufactured BP; reaction path of H formation; NMR and FTIR spectra of H; UV–vis spectra of Cy5.5-labeled PD-L1; DLS size distribution of BP@DHC and BP@DHCA; EDX map of BP@DHCA; FACS result for CD8+ isolation; uptake of BP@DHC and BP@DHCA into HCT-116 and CD8+ T cells; cytotoxicity of BP@DHCA on CD8+ T cells; FACS result for analyzing bindings between PD-L1 inhibitor peptide and PD-L1; ex vivo biodistribution of free Cy5.5; in vivo photothermal effect; digital image of treated mice; DLS size distribution, ζ -potential, D loading efficiency of BP@DHCA; histomorphometrical analysis of treated mice; and a video clip of NIR irradiation on tumor area (PDF)

In vivo photothermal effect of BP@DHCA (MP4)

AUTHOR INFORMATION

Corresponding Authors

*E-mail: postjb@yu.ac.kr (J.H.B.).

*E-mail: jongohkim@yu.ac.kr (J.O.K.).

ORCID

Jeong Hoon Byeon: 0000-0003-0903-7128

Jong Oh Kim: 0000-0002-4929-851X

Notes

The authors declare no competing financial interest.

ACKNOWLEDGMENTS

This work was supported by the NRF of Korea Grant funded by the Korean Government (NRF-2018R1A2A2A05021143). This research was also supported by the Medical Research Center Program (2015R1A5A2009124) through the NRF funded by MSIP.

REFERENCES

- (1) Hassan, S.; Prakash, G.; Ozturk, A. B.; Saghazadeh, S.; Sohail, M. F.; Seo, J.; Dokmeci, M. R.; Zhang, Y. S.; Khademhosseini, A. Evolution and Clinical Translation of Drug Nanomaterials. *Nano Today* **2017**, *15*, 91–106.
- (2) Lin, G.; Mi, P.; Chu, C.; Zhang, J.; Liu, G. Inorganic Nanocarriers Overcoming Multidrug Resistance for Cancer Therapeutics. *Adv. Sci.* **2016**, *3*, No. 1600134.
- (3) Gai, S.; Yang, G.; Yang, P.; He, F.; Lin, J.; Jin, D.; Xing, B. Recent Advances in Functional Nanomaterials for Light-Triggered Cancer Therapy. *Nano Today* **2018**, *19*, 146–187.
- (4) Liu, Q.; Zhan, C.; Kohane, D. S. Phototriggered Drug Delivery Using Inorganic Nanomaterials. *Bioconjugate Chem.* **2017**, *28*, 98–104.
- (5) Chen, Y.; Wang, L.; Shi, J. Two-Dimensional Non-Carbonaceous Materials-Enabled Efficient Photothermal Cancer Therapy. *Nano Today* **2016**, *11*, 292–308.
- (6) Li, M.; Luo, Z.; Zhao, Y. Self-Assembled Hybrid Nanostructures: Versatile Multifunctional Nanoplatfoms for Cancer Diagnosis and Therapy. *Chem. Mater.* **2018**, *30*, 25–53.
- (7) Wang, Y.; Wang, F.; Shen, Y.; He, Q.; Guo, S. Tumor-Specific Disintegratable Nanohybrids Containing Ultrasmall Inorganic Nanoparticles: From Design and Improved Properties to Cancer Applications. *Mater. Horiz.* **2018**, *5*, 184–205.
- (8) Cassano, D.; Pocić-Martínez, S.; Voliani, V. Ultrasmall-in-Nano Approach: Enabling the Translation of Metal Nanomaterials to Clinics. *Bioconjugate Chem.* **2018**, *29*, 4–16.
- (9) Yang, G.; Wan, X.; Gu, Z.; Zeng, X.; Tang, J. Near Infrared Photothermal-Responsive Poly(vinylalcohol)/Black Phosphorus Composite Hydrogels with Excellent On-Demand Drug Release Capacity. *J. Mater. Chem. B* **2018**, *6*, 1622–1632.
- (10) Qiu, M.; Wang, D.; Liang, W.; Liu, L.; Zhang, Y.; Chen, X.; Sang, D. K.; Xing, C.; Li, Z.; Dong, B.; Xing, F.; Fan, D.; Bao, S.; Zhang, H.; Cao, Y. Novel Concept of the Smart NIR-Light-Controlled Drug Release of Black Phosphorus Nanostructure for Cancer Therapy. *Proc. Natl. Acad. Sci. U.S.A.* **2018**, *115*, 501–506.
- (11) Mu, X.; Wang, J.-Y.; Bai, X.; Xu, F.; Liu, H.; Yang, J.; Jing, Y.; Liu, L.; Xue, X.; Dai, H.; Liu, Q.; Sun, Y.-M.; Liu, C.; Zhang, X.-D. Black Phosphorus Quantum Dot Induced Oxidative Stress and Toxicity in Living Cells and Mice. *ACS Appl. Mater. Interfaces* **2017**, *9*, 20399–20409.
- (12) Qian, X.; Gu, Z.; Chen, Y. Two-Dimensional Black Phosphorus Nanosheets for Theranostic Nanomedicine. *Mater. Horiz.* **2017**, *4*, 800–816.
- (13) Yang, X.; Wang, D.; Shi, Y.; Zou, J.; Zhao, Q.; Zhang, Q.; Huang, W.; Shao, J.; Xie, X.; Dong, X. Black Phosphorus Nanosheets Immobilizing Ce6 for Imaging-Guided Photothermal/Photodynamic Cancer Therapy. *ACS Appl. Mater. Interfaces* **2018**, *10*, 12431–12440.
- (14) Wang, H.; Zhong, L.; Liu, Y.; Xu, X.; Xing, C.; Wang, M.; Bai, S.-M.; Lu, C.-H.; Yang, H.-H. A Black Phosphorus Nanosheets-Based siRNA Delivery System for Synergistic Photothermal and Gene Therapy. *Chem. Commun.* **2018**, *54*, 3142–3145.
- (15) Chen, L.; Chen, C.; Chen, W.; Li, K.; Chen, X.; Tang, X.; Xie, G.; Luo, X.; Wang, X.; Liang, H.; Yu, S. Biodegradable Black Phosphorus Nanosheets Mediate Specific Delivery of hTERT siRNA for Synergistic Cancer Therapy. *ACS Appl. Mater. Interfaces* **2018**, *10*, 21137–21148.
- (16) Guiney, L. M.; Wang, X.; Xia, T.; Nel, A. E.; Hersam, M. C. Assessing and Mitigating the Hazard Potential of Two-Dimensional Materials. *ACS Nano* **2018**, *12*, 6360–6377.
- (17) Guo, T.; Wu, Y.; Lin, Y.; Xu, X.; Lian, H.; Huang, G.; Liu, J.-Z.; Wu, X.; Yang, H.-H. Black Phosphorus Quantum Dots with Renal Clearance Property for Efficient Photodynamic Therapy. *Small* **2018**, *14*, No. 1702815.
- (18) Yang, X.; Liu, G.; Shi, Y.; Huang, W.; Shao, J.; Dong, X. Nano-Black Phosphorus for Combined Cancer Phototherapy: Recent Advances and Prospects. *Nanotechnology* **2018**, *29*, No. 222001.
- (19) Qiu, M.; Ren, W. X.; Jeong, T.; Won, M.; Park, G. Y.; Sang, D. K.; Liu, L.-P.; Zhang, H.; Kim, J. S. Omnipotent Phosphorene: A Next-Generation, Two-Dimensional Nanoplatfom for Multidisciplinary Biomedical Applications. *Chem. Soc. Rev.* **2018**, *47*, 5588–5601.
- (20) Xing, C.; Chen, S.; Qiu, M.; Liang, X.; Liu, Q.; Zou, Q.; Li, Z.; Xie, Z.; Wang, D.; Dong, B.; Liu, L.; Fan, D.; Zhang, H. Conceptually Novel Black Phosphorus/Cellulose Hydrogels as Promising Photothermal Agents for Effective Cancer Therapy. *Adv. Healthcare Mater.* **2018**, *7*, No. 1701510.
- (21) Couzin-Frankel, J. Cancer Immunotherapy. *Science* **2013**, *342*, 1432–1433.
- (22) Song, W.; Musetti, S. N.; Huang, L. Nanomaterials for cancer immunotherapy. *Biomaterials* **2017**, *148*, 16–30.
- (23) Wang, Z.; Liu, W.; Shi, J.; Chen, N.; Fan, C. Nanoscale Delivery Systems for Cancer Immunotherapy. *Mater. Horiz.* **2018**, *5*, 344–362.
- (24) Liang, C.; Xu, L.; Song, G.; Liu, Z. Emerging Nanomedicine Approaches Fighting Tumor Metastasis: Animal Models, Metastasis-Targeted Drug Delivery, Phototherapy, and Immunotherapy. *Chem. Soc. Rev.* **2016**, *45*, 6250–6269.
- (25) Chen, Q.; Xu, L.; Liang, C.; Wang, C.; Peng, R.; Liu, Z. Photothermal Therapy with Immune-Adjuvant Nanoparticles together with Checkpoint Blockade for Effective Cancer Immunotherapy. *Nat. Commun.* **2016**, *7*, No. 13193.
- (26) Guo, L.; Yan, D. D.; Yang, D.; Li, Y.; Wang, X.; Zalewski, O.; Yan, B.; Lu, W. Combinatorial Photothermal and Immuno Cancer Therapy Using Chitosan-Coated Hollow Copper Sulfide Nanoparticles. *ACS Nano* **2014**, *8*, 5670–5681.
- (27) Yang, C.; Wu, T.; Qi, Y.; Zhang, Z. Recent Advances in the Application of Vitamin E TPGS for Drug Delivery. *Theranostics* **2018**, *8*, 464–485.
- (28) Wang, X.; Shao, J.; Raouf, M. A. E.; Xie, H.; Huang, H.; Wang, H.; Chu, P. K.; Yu, X.-F.; Yang, Y.; Abdel-Aal, A. M.; Mekawy, N. H. M.; Miron, R. J.; Zhang, Y. Near-Infrared Light-Triggered Drug Delivery System Based on Black Phosphorus for *In Vivo* Bone Regeneration. *Biomaterials* **2018**, *179*, 164–174.
- (29) Poudel, B. K.; Hwang, J.; Ku, S. K.; Kim, J. O.; Byeon, J. H. A Batch-by-Batch Free Route for the Continuous Production of Black Phosphorus Nanosheets for Targeted Combination Cancer Therapy. *NPG Asia Mater.* **2018**, *10*, 727–739.
- (30) Cooper, Z. A.; Reuben, A.; Austin-Breneman, J.; Wargo, J. A. Does It MEK a Difference? Understanding Immune Effects of Targeted Therapy. *Clin. Cancer Res.* **2015**, *21*, 3102–3104.
- (31) Chen, Y.; Liu, Y.-C.; Sung, Y.-C.; Ramjiawan, R. R.; Lin, T.-T.; Chang, C.-C.; Jeng, K.-S.; Chang, C.-F.; Liu, C.-H.; Gao, D.-Y.; Hsu, F.-F.; Duyverman, A. M.; Kitahara, S.; Huang, P.; Dima, S.; Popescu, I.; Flaherty, K. T.; Zhu, A. X.; Bardeesy, N.; Jain, R. K.; Benes, C. H.; Duda, D. G. Overcoming Sorafenib Evasion in Hepatocellular Carcinoma Using CXCR4-Targeted Nanoparticles to Co-Deliver MEK-Inhibitors. *Sci. Rep.* **2017**, *7*, No. 44123.

- (32) Gao, D.-Y.; Lin, T.-T.; Sung, Y.-C.; Liu, Y. C.; Chiang, W.-H.; Chang, C.-C.; Liu, J.-Y.; Chen, Y. CXCR4-Targeted Lipid-Coated PLGA Nanoparticles Deliver Sorafenib and Overcome Acquired Drug Resistance in Liver Cancer. *Biomaterials* **2015**, *67*, 194–203.
- (33) Chittasupho, C.; Anuchapreeda, S.; Sarisuta, N. CXCR4 Targeted Dendrimer for Anti-Cancer Drug Delivery and Breast Cancer Cell Migration Inhibition. *Eur. J. Pharm. Biopharm.* **2017**, *119*, 310–321.
- (34) Sung, Y.-C.; Liu, Y.-C.; Chao, P.-H.; Chang, C.-C.; Jin, P.-R.; Lin, T.-T.; Lin, J.-A.; Cheng, H.-T.; Wang, J.; Lai, C. P.; et al. Combined Delivery of Sorafenib and a MEK Inhibitor Using CXCR4-Targeted Nanoparticles Reduces Hepatic Fibrosis and Prevents Tumor Development. *Theranostics* **2018**, *8*, 894–905.
- (35) Misra, A. C.; Luker, K. E.; Durmaz, H.; Luker, G. D.; Lahann, J. CXCR4-Targeted Nanocarriers for Triple Negative Breast Cancers. *Biomacromolecules* **2015**, *16*, 2412–2417.
- (36) Zhang, D.; Lin, X.; Lan, S.; Sun, H.; Wang, X.; Liu, X.; Zhang, Y.; Zeng, Y. Localized Surface Plasmon Resonance Enhanced Singlet Oxygen Generation and Light Absorption Based on Black Phosphorus@AuNPs Nanosheet for Tumor Photodynamic/Thermal Therapy. *Part. Part. Syst. Charact.* **2018**, *35*, No. 1800010.
- (37) Yang, G.; Liu, Z.; Li, Y.; Hou, Y.; Fei, X.; Su, C.; Wang, S.; Zhuang, Z.; Guo, Z. Facile Synthesis of Black Phosphorus–Au Nanocomposites for Enhanced Photothermal Cancer Therapy and Surface-Enhanced Raman Scattering Analysis. *Biomater. Sci.* **2017**, *5*, 2048–2055.
- (38) Poudel, B. K.; Hwang, J.; Ku, S. K.; Kim, J. O.; Byeon, J. H. Plug-and-Play Continuous Gas Flow Assembly of Cysteine-Inserted AuCu Nanobimetal for Folate-Receptor-Targeted Chemo-Phototherapy. *ACS Appl. Mater. Interfaces* **2019**, *11*, 17193–17203.
- (39) He, S.; Song, J.; Qu, J.; Cheng, Z. Crucial Breakthrough of Second Near-Infrared Biological Window Fluorophores: Design and Synthesis Toward Multimodal Imaging and Theranostics. *Chem. Soc. Rev.* **2018**, *47*, 4258–4278.
- (40) Wang, C.; Chen, X.; Yao, X.; Chen, L.; Chen, X. Dual Acid-Responsive Supramolecular Nanoparticles as New Anticancer Drug Delivery Systems. *Biomater. Sci.* **2016**, *4*, 104–114.
- (41) Kumari, S.; Ram, B.; Kumar, D.; Ranote, S.; Chauhan, G. S. Nanoparticles of Oxidized-Cellulose Synthesized by Green Method. *Mater. Sci. Energy Technol.* **2018**, *1*, 22–28.
- (42) Hu, J.; Miura, S.; Na, K.; Bae, Y. H. pH-Responsive and Charge Shielded Cationic Micelle of Poly(l-histidine)-Block-Short Branched PEI for Acidic Cancer Treatment. *J. Controlled Release* **2013**, *172*, 69–76.
- (43) Wu, Q.; Liang, M.; Zhang, S.; Liu, X.; Wang, F. Development of Functional Black Phosphorus Nanosheets with Remarkable Catalytic and Antibacterial Performance. *Nanoscale* **2018**, *10*, 10428–10435.
- (44) Ouyang, J.; Deng, L.; Chen, W.; Sheng, J.; Liu, Z.; Wang, L.; Liu, Y.-N. Two Dimensional Semiconductors for Ultrasound-Mediated Cancer Therapy: The Case of Black Phosphorus Nanosheets. *Chem. Commun.* **2018**, *54*, 2874–2877.
- (45) Nguyen, H. T.; Tran, K. K.; Sun, B.; Shen, H. Activation of Inflammasomes by Tumor Cell Death Mediated by Gold Nanoshells. *Biomaterials* **2012**, *33*, 2197–2205.
- (46) Emens, L. A.; Middleton, G. The Interplay of Immunotherapy and Chemotherapy: Harnessing Potential Synergies. *Cancer Immunol. Res.* **2015**, *3*, 436–443.
- (47) Liang, X.; Ye, X.; Wang, C.; Xing, C.; Miao, Q.; Xie, Z.; Chen, X.; Zhang, X.; Zhang, H.; Mei, L. Photothermal Cancer Immunotherapy by Erythrocyte Membrane-Coated Black Phosphorus Formulation. *J. Controlled Release* **2019**, *296*, 150–161.
- (48) Tao, W.; Zhu, X.; Yu, X.; Zeng, X.; Xiao, Q.; Zhang, X.; Ji, X.; Wang, X.; Shi, J.; Zhang, H.; Mei, L. Black Phosphorus Nanosheets as a Robust Delivery Platform for Cancer Theranostics. *Adv. Mater.* **2017**, *29*, No. 1603276.
- (49) Ou, W.; Byeon, J. H.; Thapa, R. K.; Ku, S. K.; Yong, C. S.; Kim, J. O. Plug-and-Play Nanorization of Coarse Black Phosphorus for Targeted Chemo-photoimmunotherapy of Colorectal Cancer. *ACS Nano* **2018**, *12*, 10061–10074.